Supporting Information

Boosting the photocatalytic hydrogen evolution performance via an atomically thin 2D heterojunction visualized by scanning photoelectrochemical microscopy

Jae Yoon Lee[a], Sungwoo Kang[b], Donghun Lee[a], Seokhoon Choi[b], Seunghoon Yang[a], Kangwon Kim[c], Yoon Seok Kim[a], Ki Chang Kwon[b], Sooho Choi[d], Soo Min Kim[e], Jihoon Kim[f], Jungwon Park[f, g], Haeli Park[a], Woong Huh[a], Hee Seong Kang[a], Seong Won Lee[h], Hong-Gyu Park[a, h], Min Jae Ko[i], Hyeonsik Cheng[c], Seungwu Han[b, *], Ho Won Jang[b, *], and Chul-Ho Lee[a, *]

[a]KU-KIST Graduate School of Converging Science and Technology, Korea University, Seoul, 02841, Republic of Korea

[b]Department of Materials Science and Engineering, Research Institute of Advanced Materials, Seoul National University, Seoul, 08826, Korea

[c]Department of Physics, Sogang University, Seoul, 04107, Korea

[d]Department of Physics, Dongguk University, Seoul, 04620,

[e]Korea Institute of Advanced Composite Materials, Korea Institute of Science and Technology (KIST), Wanju-Gun, 55324, Korea

[f]Department of Chemical and Biological Engineering, Seoul National University, Seoul, 08826, Korea

[g]Center for Nanoparticle Research, Institute for Basic Science (IBS), Seoul, 08826, Korea

[h]Department of Physics, Korea University, Seoul, 02841, Republic of Korea

[i]Department of Chemical Engineering, Hanyang University, Seoul, 04763, Korea

*Corresponding author e-mail: chlee80@korea.ac.kr (C.-H. Lee), hwjang@snu.ac.kr (H. W. Jang), hansw@snu.ac.kr (S. Han)

Contents

S1. Device fabrication procedure

The microscale devices consist of four different kinds of layers: the monolayer MoS_2, the monolayer WS_2, the few-layer WSe_2, and the few-layer graphene. The monolayer MoS_2 was grown by chemical vapor deposition (CVD) (see the details of the growth procedure in S2), and the others were mechanically exfoliated from single crystals. All layered materials were deposited on a 285-nm-thick SiO_2-coated Si substrate and sequentially transferred onto the target SiO_2/Si substrate with prepatterned contact pads.

A total of 12 contact pads were fabricated via conventional photolithography and metal deposition (Cr/Au (5/50 nm)) processes on the 285-nm-thick SiO_2-coated Si substrate. The square area of 200×200 μm^2 was defined at the center of the contact pads, where we fabricated the devices. First, we transferred the few-layer graphene onto the prepatterned substrate to act as the bottom electrode for the transition metal dichalcogenide (TMD) heterojunction photocathode [1]. For this purpose, we used a typical polymer-assisted mechanical transfer method. To prepare a polymer supporting layer, 15 g of poly-propylene (PPC) was dissolved in 100 mL of anisole with a stirring bar at 300 rpm at 60 ℃ for 18 hours. The prepared PPC solution was spin-coated (1000 rpm for 30 s and then 3000 rpm for 5 s) on the few-layer graphene deposited substrate, followed by heating on a hot plate at 60 ℃ for 1 min to achieve intimate adhesion. Next, the polydimethyl siloxane (PDMS) stamp was brought into conformal contact with the PPC-coated graphene on the substrate. Except for the part covered with the PDMS, the remaining PPC was removed by a blade to expose the hydrophilic SiO_2 surface. After the above sample was immersed in deionized (DI) water for 3 hours, the hydrophobic PPC layer and hydrophilic SiO_2 substrate were separated by touching with a tweezer (our transfer method is similar to methods previously reported [2, 3]). The graphene/PPC/PDMS stamp was dried in an oven at 60 ℃ for 10 min, then attached to a slide glass. We attached the

inverted graphene/PPC/PDMS stamp to a micromanipulator and transferred the PPC/graphene into the center area of the prepatterned substrate by melting the PPC film at 120 ℃.

After dissolving the PPC film in acetone, to connect the few-layer graphene with one of the contact pads, we performed *e*-beam lithography using methylmethacrylate (MMA) and poly(methylmethacrylate) (PMMA) as e-beam resists, followed by metal deposition of Au/Pd/Cr (40/15/3 nm) using an e-beam evaporator.

For the fabrication of the TMD heterojunction photocathode, the mechanically exfoliated ~80-nm-thick WSe_2 and monolayer WS_2 layers were sequentially aligned and transferred by the same method as above. We finally transferred a CVD-grown single-crystalline monolayer MoS_2 flake large enough to fully cover the entire area of the pretransferred WS_2 layer. As a result, the fabricated heterostructure had three spatially distinct regions: $MoS_2/WS_2/WSe_2$, MoS_2/WSe_2, and WSe_2 (Fig. 1a).

After completing the device fabrication, to define the active area being exposed to the electrolyte solution in the following PEC measurements, we opened the areas of interest via additional e-beam lithography. Note that the PMMA layer acts as an electrical passivation layer [4-6]. The fabrication procedure is schematically shown in Fig. S1.

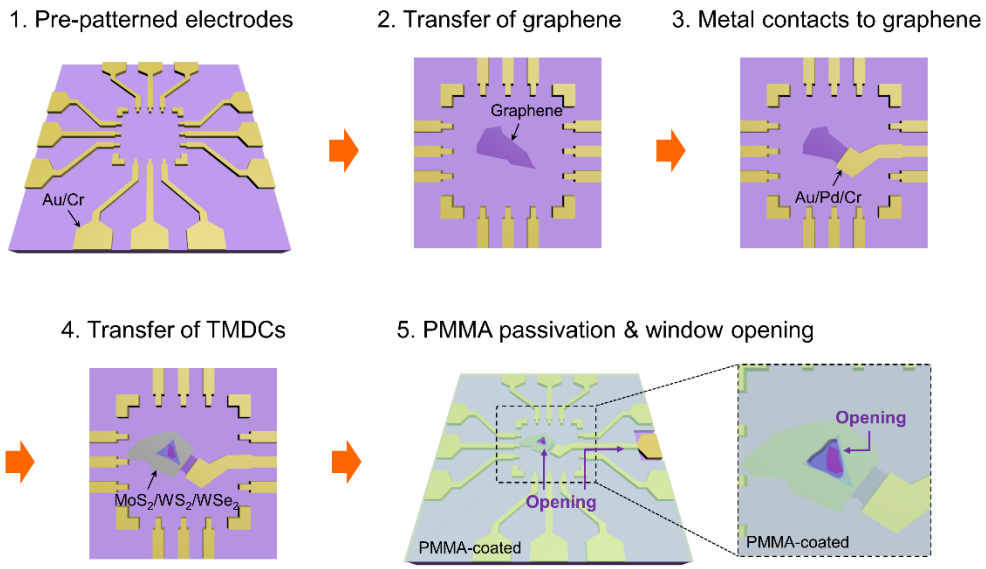

Fig. S1. Schematic illustration of the fabrication procedures.

S2. Growth of single-crystalline monolayer MoS_2 using CVD

Large-area monolayer MoS_2 flakes were grown by CVD using sodium molybdate (Na_2MoO_4, powder, 98.0 %), molybdenum hexacarbonyl ($Mo(CO)_6$, powder, 99.9 %) and dimethyl disulfide (DMDS, solvent, 99.0 %) from Sigma-Aldrich as precursors. DI water was used to prepare aqueous solutions of Na_2MoO_4 as the molybdenum source.

A 285-nm-thick SiO_2/Si substrate was treated with 0.5 M sodium hydroxide (NaOH) to increase its hydrophilicity, then rinsed with DI water and dried with a N_2 gun. Then, a 0.01 M aqueous solution of Na_2MoO_4 (molybdenum precursor) was spun onto the NaOH-treated SiO_2/Si substrate. The furnace consisted of a 2-inch quartz tube connected to a quartz bubbler containing a homogeneous mixture of 1 wt % $Mo(CO)_6$ dissolved in DMDS as the sulfur source. The coated substrate was then placed on the center of a 5 × 5 cm^2 quartz plater sample holder, with 350 and 15 sccm of Ar and H_2, respectively, used in the purging system. The quartz tube was rapidly heated to 850 °C for 10 min in a preheated furnace. The growth of MoS_2 was carried out at 850 °C under inert atmosphere (350 sccm of Ar) for 20 min with 15 and 5 sccm of H_2 and DMDS, respectively. After growth, the quartz tube was rapidly cooled to room temperature with the aid of a standing fan for 20 min. An optical image and the Raman spectrum of the single-crystalline monolayer MoS_2 are shown in Fig. S2.

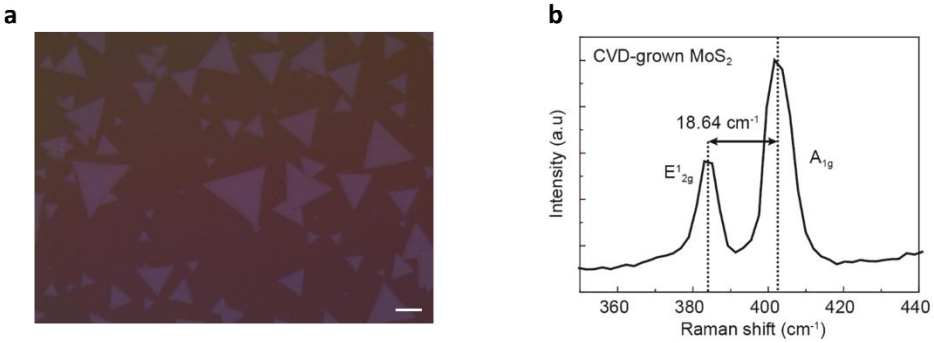

Fig. S2. (a) Optical image and (b) Raman spectrum of the CVD-grown monolayer MoS_2 on the 285-nm SiO_2/Si substrate. The frequency difference of 18.64 cm^{-1} between the E^1_{2g} and A_{1g} modes indicates that the synthesized MoS_2 is monolayer. Scale bar is 10 μm.

S3. Material characterization

Raman and PL spectra were obtained using a home-built spectrometer equipped with a monochromator (Andor, SOLIS 303i) and an excitation laser of 532 nm. The power of the excitation laser was kept below 0.2 mW to avoid damage to the materials. The radius of the focused beam was ~0.5 μm. The signal was collected by an objective lens (NIKON 100×, N.A. = 0.9) and dispersed by 1,200 and 300 line mm^{-1} grating for Raman and PL measurements, respectively.

Non-contact-mode atomic force microscopy (AFM) (Park systems, XE-10) was performed at a scanning rate of 0.5 Hz to identify the surface morphology and thickness of each layer of the TMDs and graphene. Using AFM with a conducting cantilever tip, scanning Kelvin probe microscopy (SKPM) was performed to measure the surface potentials of the differently stacked heterostructures.

Reflection measurements were performed at room temperature using broadband emission from a supercontinuum laser (Fianium, sc-400), in conjunction with a beam splitter and an objective lens (50×, N.A. = 0.8). The reflected light was dispersed by a monochomator (Horiba, TRIAX320) and detected by a thermo-electric cooled Si charge-coupled device array (Andor).

X-ray photoelectron spectroscopy (XPS) measurements were performed using an X-tool (ULVAC-PHI) with Al K_α X-ray source (1486.6 eV, 24.1 W, and 15 kV) under the ultrahigh vacuum chamber with the base pressure of ~10^{-10} Torr.

S4. Identification of the thicknesses of monolayers MoS_2 and WS_2 using AFM

Fig. S3a and S3b show AFM images and height profiles of CVD-grown monolayer MoS_2 and the exfoliated monolayer WS_2. Their thicknesses are about 0.7 nm, as previously reported in monolayer TMDs. We also confirmed the monolayer characteristics by Raman and PL spectra (Fig. 1d and S2b).

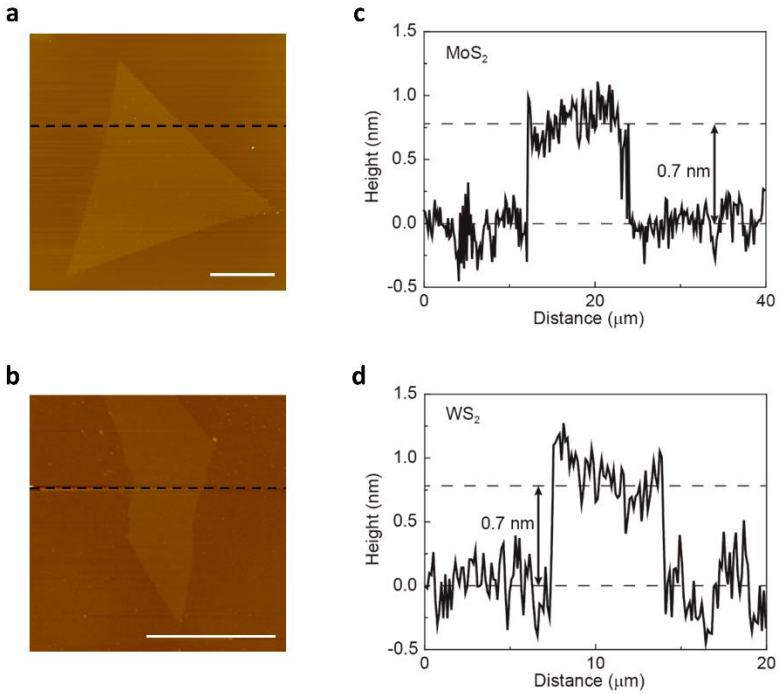

Fig. S3. (a, b) Topography images of the CVD-grown monolayer MoS_2 and exfoliated monolayer WS_2 on the 285-nm SiO_2/Si substrate, respectively. (c, d) Line profiles along the black dashed line in the topography images, respectively. Scale bars in (a) and (b) are 10 μm.

S5. Surface potential measurement using SKPM

SKPM probes the local electrical properties such as surface potential by measuring the contact potential difference between a conducting cantilever tip and a sample. The V_{CPD} (contact potential difference) is

$$V_{CPD} = \frac{\emptyset_{tip} - \emptyset_{sample}}{-q}, \quad (1)$$

where $\emptyset_{tip}$ and $\emptyset_{sample}$ are the work functions of the tip and sample, respectively, and q is the electron charge. When the tip and sample are close enough for electron tunneling, the fermi energy levels are aligned equally through electron current flow. As a result, V_{CPD} is equal to the work function difference between the tip and the sample. The work function of the sample can be extracted by measuring the V_{CPD} using a tip with the calculated work function (4.90 eV) [7].

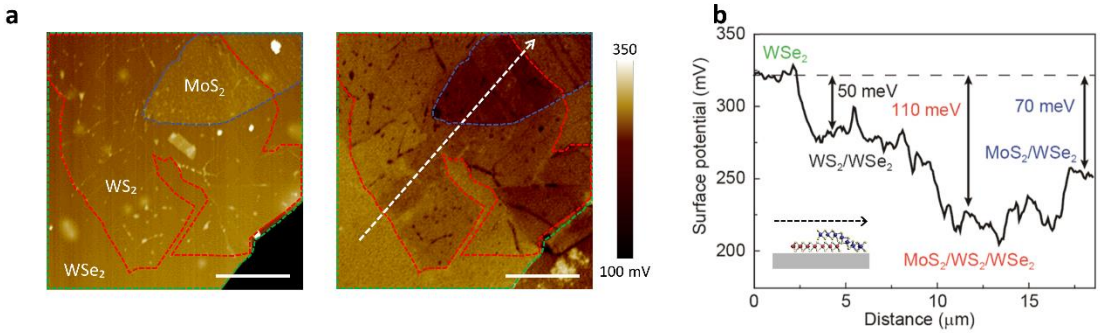

Fig. S4. (a) Topography (left) and surface potential (right) images of the $MoS_2/WS_2/WSe_2$ heterostructures. Blue, red, and green dashed lines indicate the boundaries of MoS_2, WS_2, and WSe_2, respectively. Scale bars are 5 μm. (b) Line profile of surface potential along the white dashed arrow in the surface potential image of (a). Inset: A schematic side view of the heterostructure along the arrow.

Fig. S4a shows topography and surface potential images of the $MoS_2/WS_2/WSe_2$ heterostructure. In particular, the differently stacked areas are distinguished in the surface potential image. The V_{CPD} of the bare WSe_2 surface is the largest, and that of the MoS_2/WS_2 heterojunction area is the smallest. As shown in Fig. S4b, we also plotted the line profile of the surface potential along the white dashed arrow in the surface potential image. The calculated work function of the few-layer WSe_2 is ~4.57 eV, similar to the previously reported value [8]. The surface potential differences are 70 and 110 meV for MoS_2 and MoS_2/WS_2 on the WSe_2 layers, respectively. These increases in surface potential difference (, which is proportional to work function) indicate that charge-transfer processes and shifting of the fermi energy level occur within the fabricated TMD heterojunctions, as observed in the PL measurements and assumed in the theoretical calculations. Notably, that of the MoS_2 is the same, but the surface potential difference of the MoS_2 in the type-II cascade band structure is larger than that of the MoS_2 stacked on the WSe_2 layer. This difference results in the large built-in potential at the vacuum level theoretically modeled by the first-principles calculation (see Fig. 4 in the main manuscript).

S6. Absorption measurements of the $MoS_2/WS_2/WSe_2$ heterostructures

Absorption measurements of two-dimensional materials such as graphene and TMDs with atomic thickness ($d \ll \lambda$) could be performed by comparing the reflectance spectrum of the material on a thick transparent quartz substrate (R_{m+s}) with that of the bare substrate (R_s) [9]. The reflectance difference (δ_R) obtained by solving the Maxwell's equations is expressed by

$$\delta_R = \frac{R_{m+s} - R_s}{R_s} = \frac{4}{{n_s}^2 - 1}\mathrm{A}, \qquad (2)$$

where n_s is the refractive index of the underlying substrate, and A is the absorbance. Therefore, the absorbance (A) is proportional to the reflectance difference (δ_R).

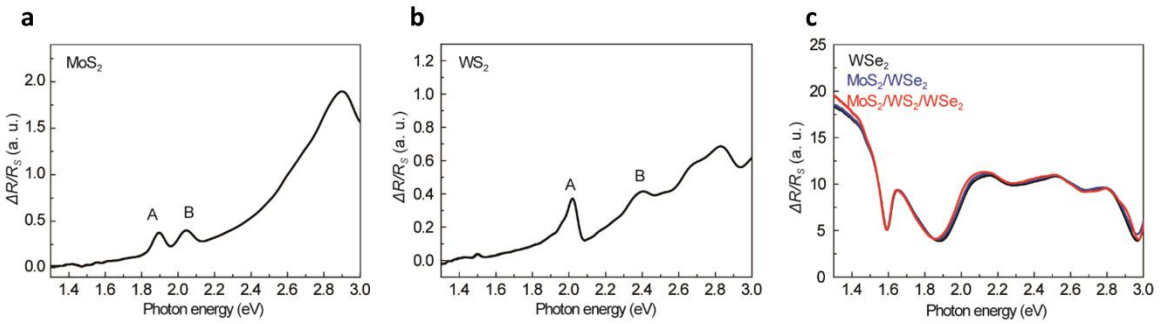

Fig. S5. Measured reflectance difference spectra of (a) the monolayer MoS_2, (b) the monolayer WS_2, (c) the 80nm-thick WSe_2 (black line), MoS_2/WSe_2 (blue line), and $MoS_2/WS_2/WSe_2$ (red line). All spectra were obtained by comparing with reflectance of the quartz substrate (R_s) as a reference.

Fig. S5a and S5b show measured reflectance difference spectra of the monolayer MoS_2 and the monolayer WS_2. A and B exciton peaks for monolayers, corresponding to MoS_2 (1.85 and 2.05 eV) and WS_2 (2.00 and 2.40 eV), were clearly observed, similar to the previously reported value [10]. Fig. S5c shows reflectance difference spectra of the 80nm-thick WSe_2, MoS_2/WSe_2, and $MoS_2/WS_2/WSe_2$, which obtained by comparing with that of the quartz substrate (R_s).

Those spectra measured from three different structures are almost identical, meaning that the contributions of atomically thin MoS_2 and WS_2 in light absorption are negligible.

S7. X-ray photoelectron spectroscopy measurement of the MoS_2/WS_2 heterostructure

We performed X-ray photoelectron spectroscopy (XPS) measurements for the chemical-vapor-deposited monolayer MoS_2, WS_2, and the stacked MoS_2/WS_2 heterostructure, which are available at the wafer scale. As shown in Fig. S6a-c, XPS peaks at 231.9, 228.7, 225.9, 34.4, 32.4, 162.05, and 161.8 eV measured from individual MoS_2 and WS_2 are attributed to the Mo $3d_{3/2}$, Mo $3d_{3/2}$, S 2s, W $5p_{3/2}$, W $4f_{5/2}$, W $4f_{7/2}$, S $2p_{1/2}$, and S $2p_{3/2}$ levels, respectively. When the heterostructure is formed, peak shifts toward lower binding energies of -125, -375, and -200 meV are observed for Mo 3d, W 4f, and S 2p core levels, respectively. These peak shifts are understood by Fermi-level (E_F) realignment to adjust the initial E_F difference between MoS_2 and WS_2 [11]. It also indicates that both MoS_2 and WS_2 have net negative charges in the heterostructure due to intrinsic *n*-type characteristics of both layers. The XPS results suggest that the chemical and/or structural interaction do not take place, but the interlayer charge transfer induced by E_F difference occurs in the heterostructure. Note that the charge transfer process can be different depending on composition and band alignment of the heterostructure as well as relative doping of constituent layers.

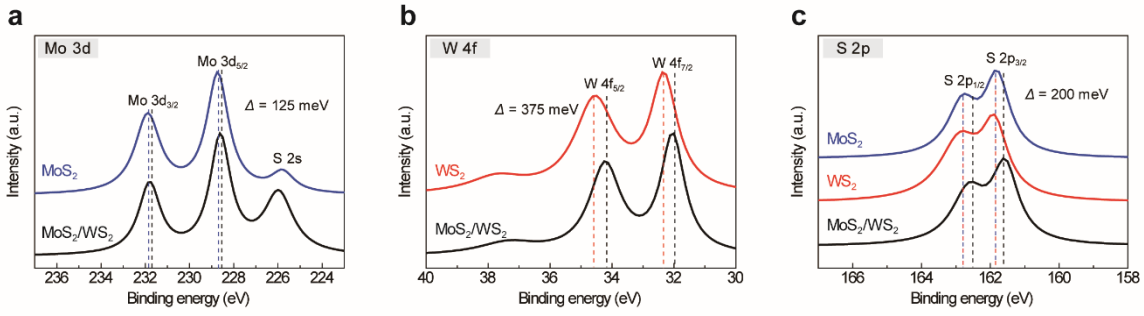

Fig. S6. XPS spectra of (a) Mo 3d, (b) W 4f, (c) S 2p core levels measured from the MoS_2/WS_2 heterostructure (black solid line), monolayer MoS_2 (blue solid line), and monolayer WS_2 (red solid line), respectively.

S8. Photoelectrochemical characterization

All PEC measurements were performed by an Ivium potentiostat (Ivium Technologies, Compact-stat) with a three-electrode system using a Pt wire counter electrode, a saturated calomel reference electrode, and a working electrode in a 0.5 M H_2SO_4 standard electrolyte solution. The three-electrode system was built inside a home-designed reaction bath. The specific areas in the microscale device were exposed by *e*-beam lithographic patterning.

S8-1. Spatially resolved PEC measurements using scanning photocurrent microscopy

For this particular characterization, we opened all the different catalytic surfaces of interest at once. A 532 nm laser was focused on the surface by a long-working-distance objective lens (Mitutoyo, M Plan Apo SL 100×, N.A. = 0.55, W.D. = 13 mm). The incident laser power was ~0.1 μW measured using a power meter (Newport, Ophir 7Z01500 Nava) and the focused laser spot size was ~1 μm in diameter. The focused laser spot was scanned using a microstage or Galvano mirrors. Photocurrent was measured at constant voltage (0 V vs. RHE) and converted to voltage signal using a break out box (Ivium Technologies, Peripheral Port Expender) and a lock-in amplifier (Stanford Research Systems, SR830) at an optical chopping frequency of ~100 Hz.

S8-2. Spatially defined PEC measurements using a solar simulator

We defined a circular hole pattern (radius = 2 μm) to expose only the area of interest for spatially defined PEC measurements. The measurement was performed under 1 Sun (AM 1.5 G condition). A Xe arc lamp was used as an illumination source and calibrated to an output power of 100 mW cm^{-2} using a Si reference cell. A scan rate of 10 mV s^{-1} was used for the linear sweep. Electrochemical impedance spectroscopy (EIS) was conducted by applying a constant potential of -0.14 V vs. RHE. The sweeping frequency was from 350 kHz to 0.1 Hz.

S9. Additional PEC mapping results for different device structures

In the main manuscript, we reported photocurrent mapping experiments of the device with a lithographic opening that contained only the MoS_2 and MoS_2/WS_2 regions to reveal solely the effects of the heterojunction on the HER compared to those of the single layer (Fig. 2f). Additionally, as presented in Fig. S6 and S7, we carried out photocurrent mapping for other devices to show that the scanning PEC mapping technique developed here works versatilely for the spatially resolved characterization and visualization of the photocatalytic activities of various active sites and heterostructures.

S9-1. Heterojunctions with different thicknesses of WS_2

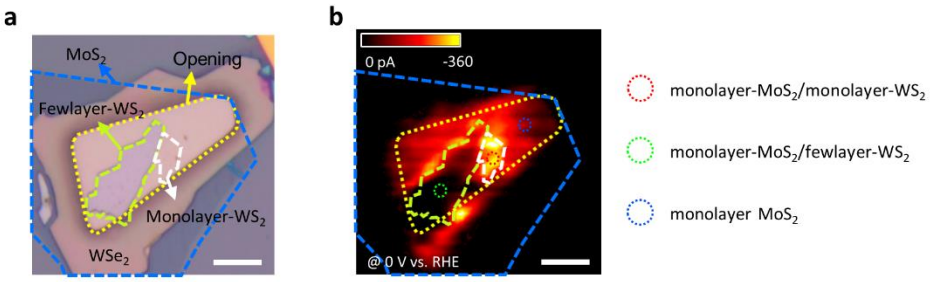

Fig. S7. Spatially resolved PEC characterization of the MoS_2/WS_2 heterojunction catalyst with different thicknesses of WS_2. (a, b) Optical and photocurrent mapping images of the microfabricated device. The lithographic opening area (indicated by the yellow dotted line) exposes the MoS_2 basal surfaces of the monolayer MoS_2, the monolayer-MoS_2/monolayer-WS_2 heterojunction, and the monolayer-MoS_2/fewlayer-WS_2 heterojunction on the WSe_2 layers. The boundaries of monolayer MoS_2, monolayer WS_2, and few-layer WS_2 are indicated by blue, white, and light green dashed lines, respectively. The photocurrent mapping image is obtained by using a focused 532 nm laser at 0.0 V vs RHE. Scale bars are 10 μm.

As shown in Fig. S7, we fabricated a device including the MoS_2/WS_2 heterojunction with different thicknesses of WS_2. Note that the edges of MoS_2 and the basal surface of WSe_2 are

not exposed in this device. For the area of the monolayer-MoS_2/monolayer-WS_2 heterojunction, as in the device shown in Fig. 2 of the main manuscript, a larger photocurrent is obtained than on the monolayer MoS_2. On the other hand, the photocurrent measured from the monolayer-MoS_2/fewlayer-WS_2 heterojunction area is even smaller than that from the basal MoS_2 plane. This result can be explained by the large resistance of charge transport by hopping over multiple interlayer potential barriers in the layered structure[12].

S9-2. Heterojunction *vs.* Edge

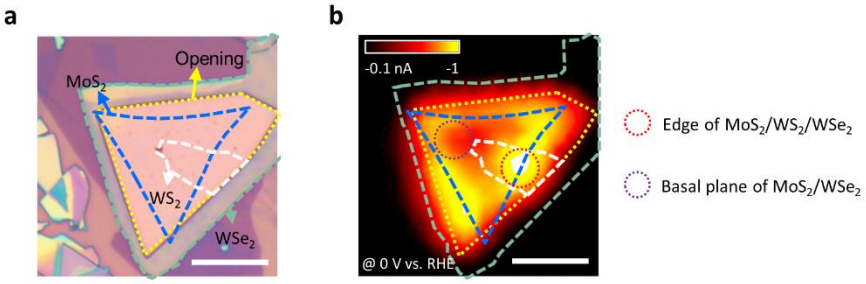

Fig. S8. Spatially resolved PEC characterization of an active area including the edge of MoS_2 as well as the basal plane and the heterojunction structures. (a, b) Optical and photocurrent mapping images of the microfabricated device. The lithographic opening area (indicated by the yellow dotted line) exposes the edges of MoS_2, the bare surface of WSe_2 (no catalyst), the monolayer MoS_2 on WSe_2, and the MoS_2/WS_2 heterojunction on WSe_2. The boundaries of MoS_2, WS_2, and WSe_2 are indicated by the blue, white, and green dashed lines, respectively. The photocurrent mapping image is obtained by using a focused 532 nm laser at 0 V vs. RHE. Scale bars are 10 μm.

As another example shown in Fig. S8, in contrast to the one presented in Fig. 2 of the main manuscript, the lithographic opening area is larger than the CVD-grown monolayer MoS_2 and thus includes the edges of MoS_2 and the bare surface of WSe_2 as well as the heterojunctions. In the photocurrent map, a relatively large current is observed predominantly from the edges

of MoS_2, reflecting that the HER is more active on the edges than at other active sites including the basal surfaces of MoS_2 and WSe_2. This result is quite consistent with previously reported results [5], strongly suggesting that the spatially resolved PEC characterization works well. However, the exposure of the edges makes it difficult to differentially reveal the effect of the heterojunction on the HER, which needs to be clarified in this work. Interestingly, however, the largest photocurrent is measured at the MoS_2 edge located on the monolayer WS_2, presumably due to the combined contribution of the edge and the heterojunction [5, 13].

S10. Raman spectra before and after PEC characterization

To investigate the stability of the catalyst during a series of PEC measurements including SPECM, we performed the Raman characterization before and after the measurements. As shown in Fig. S9, the resonance Raman peaks of each MoS_2, WS_2 and WSe_2 layer were clearly observed without noticeable degradation and shift before and after measurements, indicating that the structure and composition of the catalyst are maintained during PEC measurements.

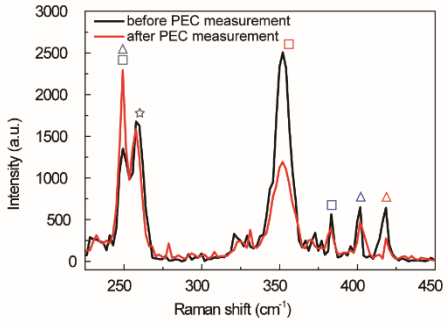

Fig. S9. Raman spectra of the $MoS_2/WS_2/WSe_2$ heterostructure before (black solid line) and after (red solid line) PEC characterization. Squares, triangles, and a star in gray (WSe_2), red (WS_2), and blue (MoS_2) represent the E^1_{2g}, A_{1g}, and 2LA(M) modes respectively.

S11. Electrochemical hydrogen evolution reaction characteristics

The hydrogen evolution reaction (HER) takes place through three principal steps [14]. The first is the Volmer reaction, which is the electrochemical adsorption of hydrogen ion on the catalyst surface (M), while the other two steps correspond to the desorption of adsorbed hydrogen (H_{ad}). The atomic adsorbed hydrogen desorbs via either electrochemical desorption, known as the Heyrovsky reaction, or chemical desorption, known as the Tafel reaction. A step-by-step description of the HER is shown below [15]:

$$M + H_3O^+ + e^- \rightarrow M\text{-}H_{ad} + H_2O \text{ (Volmer reaction)} \quad (3)$$

$$H_3O^+ + e^- + M\text{-}H_{ad} \rightarrow M + H_2 + H_2O \text{ (Heyrovsky reaction)} \quad (4)$$

$$M\text{-}H_{ad} + M\text{-}H_{ad} \rightarrow 2M + H_2 \text{ (Tafel reaction)} \quad (5)$$

The combination of steps (3) and (4) or of steps (3) and (5) can lead to the production (recombination) of molecular H_2. To identify the HER mechanism, the HER activity is evaluated by the rate-determining step determined from the Tafel slope. If the rate-determining step is the Volmer reaction, the Tafel slope is ~118 mV dec^{-1}; if the rate-determining step is the Heyrovsky reaction, the value is ~39 mV dec^{-1}; and if the rate-determining step is the Tafel reaction, the value is 29 mV dec^{-1}. The Tafel slope is the slope of the linear portion of the curve, in which the overpotential is plotted as a function of the logarithm of the current density. The Tafel slope (A) is

$$\eta = A \log(\frac{j}{j_0}), \quad (6)$$

where η, A, j, and j_0 are the overpotential, Tafel slope, current density, and exchange current density, respectively. A good electrochemical catalyst has a low Tafel slope [16].

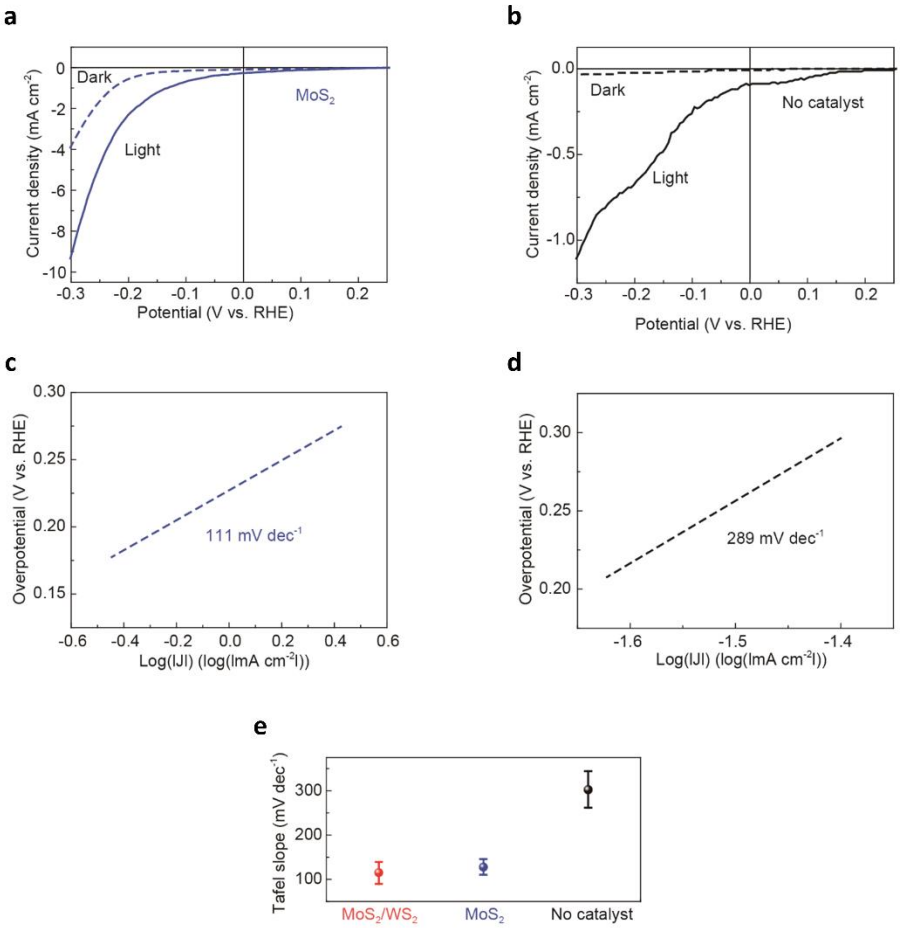

Fig. S10. Polarization curves of (a) the MoS_2/WSe_2 heterostructure and (b) the WSe_2 layer with no catalyst in the dark (dashed lines) and under 1 Sun illumination (solid lines). (c, d) Corresponding plots of Tafel slopes extracted from the curves in the dark. (e) Statistics of the Tafel slope of each structure. Red, blue, and black squares represent the MoS_2/WS_2 heterojunction, the MoS_2 single layer, and no catalyst (bare WSe_2), respectively.

To investigate the HER mechanism in our photocathode systems, we measured the HER performance in the dark and under illumination for specifically defined areas corresponding to the heterostructures of interest. As shown in Fig. S10a, the WSe_2 photocathode with the MoS_2 catalyst exhibits a smaller photoresponse than the MoS_2/WS_2 heterojunction catalyst (Fig. 3d

in the main manuscript). For the bare surface of WSe_2 with no catalyst layer, both the PEC and electrochemical performance are much poorer (Fig. S10b).

From the data measured in the dark, we extracted the Tafel slope for each structure (Fig. 3d for the MoS_2/WS_2 heterojunction, Fig. S8c for the monolayer MoS_2, and Fig. S10d for the bare surface of WSe_2 with no catalyst layer). The statistically measured values of the Tafel slope correspond to 114.5 ± 24.7, 128 ± 17.5, and 303 ± 41.0 mV dec^{-1} for the MoS_2/WS_2 heterojunction, the monolayer MoS_2, and the bare WSe_2 layer with no catalyst, respectively (Fig. S10e). The relatively large value of the Tafel slope indicates that the basal plane of WSe_2 is less active than that of MoS_2 for the HER [16]. In addition, as mentioned in the manuscript, because very similar values were estimated for the MoS_2/WS_2 heterojunction and the monolayer MoS_2, we speculated that the hydrogen absorption energy on the MoS_2 basal surface may not be significantly altered by the underlying WS_2 layer that forms the heterojunction.

S12. DFT calculation

The first-principles calculations were performed using Vienna *Ab initio* Simulation Package (VASP) [17]. The generalized gradient approximation was employed for the exchange-correlation functional for electrons and the energy cutoff for the plane-wave basis set was 300 eV. The van der Waals interaction was included empirically [18]. A vacuum slab with a thickness of 18 Å was inserted, and the dipole correction was used to remove spurious interaction within the periodic boundary condition. Because of lattice mismatch, we used 11.4 × 11.4 and 16.4 × 16.4 $Å^2$ for undoped MoS_2/WSe_2 and $MoS_2/WS_2/WSe_2$ heterostructures, respectively, by applying a lattice strain of ~0.1 %. To simulate the built-in potential as a function of doping concentration, we further expanded the lateral periodicity for MoS_2/WSe_2 and $MoS_2/WS_2/WSe_2$, and replaced Mo (W) atoms with Re (Nb) for electron (hole) doping. This substitution corresponded to a nominal doping concentration of 5.56×10^{12} cm^{-2}. For *k*-point sampling, 3 × 3 × 1 grid was used for undoped systems and reduced with respect to the supercell size for doped systems. The atomic positions including the interlayer distances of undoped systems were optimized, and we neglected atomic relaxations in the presence of dopants because they are negligible.

Supplementary References

[1] X. Cui, G.-H. Lee, Y.D. Kim, G. Arefe, P.Y. Huang, C.-H. Lee, D.A. Chenet, X. Zhang, L. Wang, F. Ye, F. Pizzocchero, B. Jessen, K. Watanabe, T. Taniguchi, D.A. Muller, T. Low, P. Kim, J. Hone, Nat. Nanotech., 10 (2015) 534-540.
[2] H. Li, J. Wu, X. Huang, Z. Yin, J. Liu, H. Zhang, ACS Nano, 8 (2014) 6563-6570.
[3] A. Gurarslan, Y. Yu, L. Su, Y. Yu, F. Suarez, S. Yao, Y. Zhu, M. Ozturk, Y. Zhang, L. Cao, ACS Nano, 8 (2014) 11522-11528.
[4] D. Voiry, R. Fullon, J. Yang, C.d.C.C. e Silva, R. Kappera, I. Bozkurt, D. Kaplan, M.J. Lagos, P.E. Batson, G. Gupta, A.D. Mohite, L. Dong, D. Er, V.B. Shenoy, T. Asefa, M. Chhowalla, Nat. Mater., 15 (2016) 1003-1009.
[5] J. Zhang, J. Wu, H. Guo, W. Chen, J. Yuan, U. Martinez, G. Gupta, A. Mohite, P.M. Ajayan, J. Lou, Adv. Mater., 29 (2017) 1701955.
[6] J. Wang, M. Yan, K. Zhao, X. Liao, P. Wang, X. Pan, W. Yang, L. Mai, Adv. Mater., 29 (2017) 1604464.
[7] W. Melitz, J. Shen, A.C. Kummel, S. Lee, Surf. Sci. Rep., 66 (2011) 1-27.
[8] K. Kim, S. Larentis, B. Fallahazad, K. Lee, J. Xue, D.C. Dillen, C.M. Corbet, E. Tutuc, ACS Nano, 9 (2015) 4527-4532.
[9] K.F. Mak, M.Y. Sfeir, Y. Wu, C.H. Lui, J.A. Misewich, T.F. Heinz, Phys. Rev. Lett., 101 (2008) 196405.
[10] Y. Li, A. Chernikov, X. Zhang, A. Rigosi, H.M. Hill, A.M. van der Zande, D.A. Chenet, E.-M. Shih, J. Hone, T.F. Heinz, Phys. Rev. B, 90 (2014) 205422.
[11] W. Yang, H. Kawai, M. Bosman, B. Tang, J. Chai, W. Le Tay, J. Yang, H.L. Seng, H. Zhu, H. Gong, Nanoscale, 10 (2018) 22927-22936.
[12] Y. Yu, S.-Y. Huang, Y. Li, S.N. Steinmann, W. Yang, L. Cao, Nano Lett., 14 (2014) 553-558.
[13] J. Shi, R. Tong, X. Zhou, Y. Gong, Z. Zhang, Q. Ji, Y. Zhang, Q. Fang, L. Gu, X. Wang, Z. Liu, Y. Zhang, Adv. Mater., 28 (2016) 10664-10672.
[14] B. Conway, B. Tilak, Electrochim. Acta, 47 (2002) 3571-3594.
[15] S. Giménez, J. Bisquert, Photoelectrochemical Solar Fuel Production, Springer, Berlin, 2016.
[16] D. Voiry, J. Yang, M. Chhowalla, Adv. Mater., 28 (2016) 6197-6206.
[17] G. Kresse, J. Furthmüller, Phys. Rev. B, 54 (1996) 11169-11186.
[18] S. Grimme, J. Antony, S. Ehrlich, H. Krieg, J. Chem. Phys., 132 (2010) 154104.